Composites Part C: Open Access 13 (2024) 100427

Contents lists available at ScienceDirect

Composites Part C: Open Access

journal homepage: www.sciencedirect.com/journal/composites-part-c-open-access

Micromechanics of $Ti_3C_2T_x$ MXene reinforced poly(vinyl alcohol) nanocomposites

Ming Dong [a,*], Yi Hu [b,c], Han Zhang [b], Emiliano Bilotti [b,d], Nicola Pugno [b,e], David Dunstan [a], Dimitrios G. Papageorgiou [b,*]

[a] School of Physical and Chemical Sciences, Queen Mary University of London, London E1 4NS, United Kingdom
[b] School of Engineering and Materials Science, Queen Mary University of London, London E1 4NS, United Kingdom
[c] School of Mechanical Engineering, Northwestern Polytechnical University, Xi'an 710072, China
[d] Department of Aeronautics, Imperial College London, South Kensington Campus, London SW7 2AZ, United Kingdom
[e] Laboratory for Bioinspired, Bionic, Nano, Meta Materials & Mechanics, Department for Civil, Environmental and Mechanical Engineering, University of Trento, Via Mesiano 77, Trento 38123, Italy

ARTICLE INFO

Keywords:
MXenes (Ti3C2Tx)
Poly(vinyl alcohol)
Nanocomposites
Raman spectroscopy
Micromechanics

ABSTRACT

The key to effective mechanical reinforcement in polymer nancomposites lies within the stress transfer mechanisms and the distribution of the nanofillers within a polymer matrix. In this work, the micromechanics of $Ti_3C_2T_x$ MXene-reinforced poly(vinyl alcohol) (PVA) nanocomposites have been studied in detail. $Ti_3C_2T_x$ MXene/PVA nanocomposites were prepared by solution blending. The spatial orientation of $Ti_3C_2T_x$ MXene in the nanocomposites was characterized by polarized Raman spectroscopy and the orientation factor was correlated to the effective Young's modulus of the flakes through well-established micromechanical theories. The mechanical properties of the nanocomposites were evaluated by tensile testing. A 27% increase in Young's modulus and a 24% improvement in tensile strength were achieved by addition of only 0.6 wt% $Ti_3C_2T_x$. Efficient stress transfer from the polymer matrix to $Ti_3C_2T_x$ MXene in bulk nanocomposites has been observed through strain-induced Raman band shifts for the first time. The effective Young's modulus of the MXene nanoplatelets was calculated to be in the order of 300 GPa, in good agreement with the values derived from the application of micromechanical models.

1. Introduction

In recent years, two-dimensional (2D) materials such as graphene [1], hexagonal boron nitride [2], molybdenum disulfide (MoS_2) [3], MXenes [4] etc., have attracted huge research interest due to their unique combination of mechanical, thermal and electrical properties [5,6]. Transition metal carbides and nitrides (MXenes) are 2D materials with a formula of $M_{n+1}X_nT_x$, where M is an early transition metal, X is carbon or nitrogen and T_x represents the functional groups on the surface of MXenes [7,8]. MXenes were first synthesized from the Ti_3AlC_2 MAX phase by the Gogotsi group in 2011, using the hydrogen fluoride (HF) etching method [9]. Since then, more than 40 MXene compositions have been fabricated, making them one of the fastest growing 2D materials families [10]. The properties of MXenes can be adapted by tuning the ratio of M and X elements, ranging from M_2X to M_3X_2 and M_4X_3, thereby providing more opportunities to synthesize MXenes based on specific application demands [11,12].

MXenes are excellent candidates for a wide range of applications, considering their electrochemical and optoelectronic properties. For example, MXenes possess metallic conductivity [13], high current breakdown density [14], and outstanding electrochemical properties [15]. MXenes also display promising performance towards energy storage and conversion [16,17], catalysis [18,19], electromagnetic interference shielding [20,21], ultraviolet shielding [22], sensors [23,24], electronics [25,26], environment [27,28], and biomedicine [29,30].

Polymers are used extensively in our daily life due to their ease of processing, low cost, low density, satisfactory mechanical properties and good resistance to corrosion. High-performing nanofillers such as graphene and carbon nanotubes [31] have been extensively used as polymer reinforcements to overcome some of their intrinsic disadvantages such as the low thermal conductivity and high flammability, to further

* Corresponding authors.
E-mail addresses: m.dong@qmul.ac.uk (M. Dong), d.papageorgiou@qmul.ac.uk (D.G. Papageorgiou).

https://doi.org/10.1016/j.jcomc.2023.100427

Available online 14 December 2023

explore applications that demand multifunctionality [32,33]. The exceptional intrinsic properties of MXene nanoplatelets make them suitable candidates for polymer reinforcement [34,35]. Additionally, due to the presence of abundant surface functional groups (-O, -OH, -F), MXenes display compatibility with water and organic solvents and can be incorporated into a variety of polymers through *ex situ* mixing or *in situ* polymerization [36]. Different interfacial interactions, such as hydrogen bonds [37], covalent bonds [38] and electrostatic interactions [39] can be formed between MXenes and polymer chains. Ling et al. [37] firstly explored the use of MXenes in polymer nanocomposites and fabricated MXene/polyvinyl alcohol (PVA) nanocomposites with high tensile strength (91 MPa, compared to 30 MPa for pure PVA), high electrical conductivity (240 S/cm) and notable volumetric capacitance (530 F/cm^3). After that, MXenes have been incorporated into many polymer matrices to fabricate nanocomposites for different applications (see review [36] and references within).

The mechanical properties of MXene-reinforced polymer composites play a vital role for structural and functional applications [40]. Experimentally, the Young's modulus of monolayer $Ti_3C_2T_x$ and $Nb_4C_3T_x$ was measured by atomic force microscopy (AFM) nanoindentation to be 333 ± 30 [41] and 386 ± 13 GPa [42], respectively, while theoretically (using molecular dynamics), the modulus of monolayer Ti_3C_2 was found almost equal to 502 GPa [43]. Quite interestingly, the in-plane stiffness and out-of-plane rigidity of MXenes increases with thickness and surface functionalization [44]. As a result, MXenes have been used as mechanical reinforcing agents in various polymers, such as epoxy resins [45,46], ultrahigh-molecular-weight polyethylene (UHMWPE) [47], thermoplastic polyurethane (TPU) [48,49] and natural rubber (NR) [50]. With the addition of 0.5 wt% Ti_3C_2, the tensile strength and storage modulus of a Ti_3C_2/TPU film increased by 47.1% and 39.8%, respectively [48]. In another study, methyltetrahydrophthalic anhydride (MTHPA) was used to facilitate the dispersion of $Ti_3C_2T_x$ in an epoxy resin and the formation of robust interfaces with the epoxy [45]. The elastic modulus and tensile strength were increased by 31% (from 2.6 to 3.5 GPa) and 51% (from 70.5 to 106.4 MPa) with only 0.2 wt% $Ti_3C_2T_x$. These studies demonstrate that mechanical reinforcement can be achieved by using MXenes even at low filler contents. However, the mechanisms of polymer reinforcement from MXenes (*e.g.* the stress transfer mechanism) and the spatial orientation of MXenes within a polymer matrix have not been examined thoroughly yet.

Raman spectroscopy has been widely used to study stress transfer mechanisms in polymer nanocomposites reinforced by nanomaterials [51,52]. The applied stress can induce changes in bond length and a subsequent shift is recorded in the characteristic Raman bands [53]. Therefore, stress transfer can be analysed by monitoring the shift of Raman peaks. For nanocarbon-reinforced nanocomposites (such as carbon nanotubes (CNTs) [54], graphene nanoplatelets (GNPs) [52] and graphene oxide (GO) [55]), the G or 2D Raman bands have been used to gain an insight into the micromechanics of composites. This technique has been extended to other nanofillers beyond carbon nanomaterials such as tungsten disulfide (WS_2) [56] and hexagonal boron nitride (hBN) [57]. In a recent study, the interfacial stress transfer from a polymer matrix (PMMA) to $Ti_3C_2T_x$ flakes was investigated by strain-induced Raman band shifts in a model nanocomposite configuration (where a $Ti_3C_2T_x$ flake was coated with a polymer layer) [58]. It was shown that MXenes with a length of 10 μm and a thickness of tens of nanometers can provide efficient mechanical reinforcement to a polymer matrix. However, Raman spectroscopy has not been used yet to gain insights into the stress transfer mechanisms in bulk MXene/polymer nanocomposites.

In this study, Raman spectroscopy was used to quantify the spatial orientation and follow the deformation of $Ti_3C_2T_x$ MXene within a poly (vinyl alcohol) matrix. The $Ti_3C_2T_x$ MXene/PVA nanocomposites were prepared by solution casting and were characterized by X-ray diffraction, tensile testing and Raman spectroscopy. From the use of micromechanical theories and the evaluation of strain-induced Raman band shifts, the efficiency of mechanical reinforcement by $Ti_3C_2T_x$ MXene was investigated in detail and is presented in the following sections.

2. Experimental section

2.1. Materials

Ti_3AlC_2 MAX powders (particle size of 38 μm, purity of 98%) were obtained from Jilin 11 Technology Co., Ltd. Lithium fluoride (LiF, 98.5% grade) powder and hydrochloric acid (HCl, ACS reagent) were purchased from Sigma-Aldrich. The PVA powder with an average molecular weight of 67,000 g/mol and degree of hydrolysis of 88% was provided by ME Scientific Engineering Ltd.

2.2. Synthesis of $Ti_3C_2T_x$ MXene nanoplatelets

The $Ti_3C_2T_x$ MXene nanoplatelets were prepared by the HF etching method [59] as illustrated in Fig. 1a. First, 1.6 g LiF was slowly dissolved in 20 ml 9 M HCl in a beaker and left under magnetic stirring for 30 min to prepare the etchant. Then, a total of 1 g Ti_3AlC_2 MAX powder was gradually added to the prepared etchant and the reaction was kept at 40 °C for 24 h under continuous stirring. The mixture was subsequently washed with deionized water via centrifugation at 3500 rpm for 5 min per cycle until the pH of the supernatant reached 6 − 7. The sediment was then collected and redispersed in DI water to start the delamination process. The mixture was mildly sonicated (60 W) for 10 min in an ice bath under Ar flow. Finally, the mixture was centrifuged at 3500 rpm for 20 min to obtain the MXene suspension. The concentration of the obtained MXene suspension was determined by vacuum filtering of a certain amount of suspension through a mixed cellulose ester (MCE) membrane with pore size of 0.22 μm. A filtered MXene film is shown in Figure S1 and the concentration of the suspension was about 3 mg/ml.

2.3. Preparation of $Ti_3C_2T_x$ MXene/PVA nanocomposites

The fabrication of $Ti_3C_2T_x$ MXene/PVA nanocomposites is presented schematically in Fig. 1b. The PVA powder was initially dissolved in DI water at 90 °C to produce a 5 wt% PVA aqueous solution. Then, the MXene suspension and the PVA solution were mixed to prepare nanocomposites with the desired MXene weight content (0.3, 0.6, 0.9 and 1.2 wt%). The mixtures were left under magnetic stirring for about 1 h at room temperature to obtain homogeneous dispersions. For mechanical testing, the $Ti_3C_2T_x$ MXene/PVA films were prepared by pouring the mixtures into petri dishes and drying at 60 °C for 24 h. For Raman measurements, 20 μl of the MXene/PVA mixture were drop cast on top of a PMMA beam and dried at 60 °C for 24 h.

2.4. Characterizations

2.4.1. X-ray diffraction

X-ray diffraction (XRD) was carried out using an Analytical X'Pert-Pro-diffractometer with a Cu-Kα radiation source. The scan was operated in 2θ geometry at the range of 5–70° in reflection mode.

2.4.2. Atomic force microscopy

Atomic force microscopy (AFM) was performed in semi-contact mode to study the morphology and thickness of exfoliated $Ti_3C_2T_x$ flakes. The samples were prepared by depositing $Ti_3C_2T_x$ diluted in DI water onto a silicon substrate and the mixture was then dried at room temperature. AFM tips with a spring constant of 42 N/m and resonant frequency of 350 kHz were used.

2.4.3. Scanning electron microscopy

The microstructure of both exfoliated MXenes and cryofractured composite samples (after immersion in liquid N_2) was observed using scanning electron microscopy (SEM, FEI Inspect-F, Netherlands) with an acceleration voltage of 5 kV.

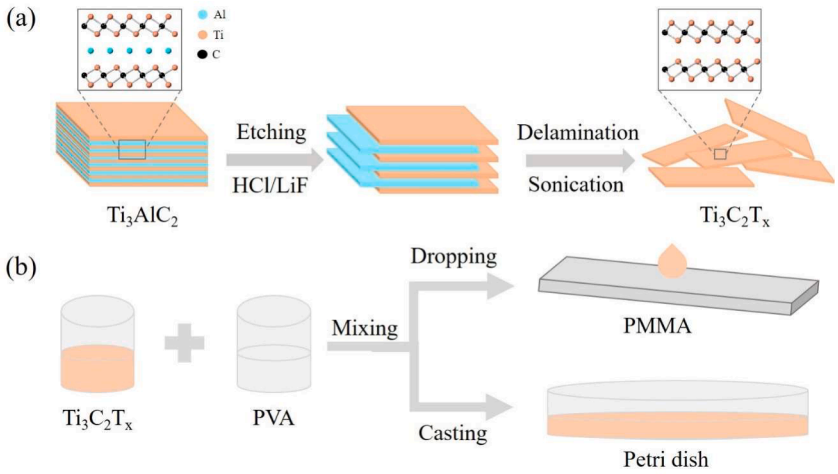

Fig. 1. (a) Liquid exfoliation of MAX Ti_3AlC_2 to MXene $Ti_3C_2T_x$. (b) Preparation of $Ti_3C_2T_x$/PVA nanocomposites. For the samples that were examined by *in situ* Raman tests, small amounts of the mixtures were dropped onto a PMMA beam; for the samples that were used for tensile tests, the mixtures were cast into a Petri dish.

2.4.4. Fourier transform infrared spectroscopy

Fourier transform infrared (FTIR) spectroscopy was used to study the functional groups of $Ti_3C_2T_x$ MXene (Bruker Tensor 27). The scanning range was 4000–1000 cm^{-1} and the resolution was 4 cm^{-1}.

2.4.5. Differential scanning calorimetry

Differential scanning calorimetry (DSC) measurements of the composite films were conducted with a TA DSC 25 under an argon flow of 20 ml/min. The sample was heated at a rate of 10 °C/min from 10 to 280 °C. The sample was held at 280 °C for 5 mins to erase the thermal history, cooled down to room temperature at 50 °C/min and then reheated at 10 °C/min to record the melting point.

2.4.6. Mechanical testing

The tensile properties of pure PVA and $Ti_3C_2T_x$/PVA nanocomposites at different loadings were studied using an Instron 5900R84. The films were cut into dogbone specimens with a gauge length of 10 mm and a width of 3 mm. The thickness of the samples was about 0.05 ± 0.01 mm. For each $Ti_3C_2T_x$/PVA nanocomposite, five samples were tested. The load cell was 100 N and the loading rate was 1 mm/min.

2.4.7. Raman spectroscopy

Raman spectroscopy data were collected using a micro-Raman spectrometer (Renishaw inVia) in a backscattering configuration. A laser excitation of 785 nm with a grating of 1200 grooves/mm was used to record the Raman signal. The laser power was kept below 1 mW to avoid laser heating effects. The exposure time was 10 s for each measurement.

Polarized Raman spectroscopy was used to determine the orientation of the MXene flakes in the polymer matrix. The VV (vertical/vertical) polarization, where the incident and scattered polarization were the same, was selected. The set-up of polarized Raman spectroscopy is illustrated in Figure S3. The $Ti_3C_2T_x$/PVA samples were placed on a rotation stage, and the laser beam was parallel to z and x directions respectively. The stage was rotated in steps of 10°.

For the *in situ* Raman deformation study, a four-point bending device was adjusted on the microscope stage. A strain gauge was attached to the centre of the beam to monitor the strain. The strain was applied to the specimen in steps of about 0.05%. Three spectra were recorded and then averaged at each strain level.

3. Results and discussion

3.1. Microstructure of $Ti_3C_2T_x$ MXene nanoplatelets

The XRD patterns of Ti_3AlC_2 MAX and $Ti_3C_2T_x$ MXene are shown in Fig. 2a. It can be seen that Ti_3AlC_2 shows the main characteristic peak from the (104) reflection at $2\theta=38.9°$, corresponding to the presence of the Al element. This peak is not observed in $Ti_3C_2T_x$ MXene, which means that the Al layer was fully etched after the *in situ* HF etching method [59]. Meanwhile, the (002) peak of Ti_3AlC_2 at 9.59° moved to 7.12° for $Ti_3C_2T_x$. This indicates that the d-spacing increased from 0.92 nm to 1.24 nm due to the presence of Li^+. In addition, four more minor peaks corresponding to reflections from (004), (006), (008) and (010) crystal planes were also observed for $Ti_3C_2T_x$.

The Raman spectra of Ti_3AlC_2 and $Ti_3C_2T_x$ are shown in Fig. 2b. The feature peaks of both Ti_3AlC_2 and $Ti_3C_2T_x$ lie in the 100−800 cm^{-1} range. The out-of-plane A_{1g} (Ti, Al) peak, ω_4, of Ti_3AlC_2 MAX moved to lower wavenumber for $Ti_3C_2T_x$ MXene (A_{1g} (Ti, O, C) in Fig. 2b) as Al was etched away and C and surface groups were involved in vibration [60]. Additionally, another out-of-plane peak of Ti_3AlC_2 (ω_6) moved to higher wavenumber in the case of $Ti_3C_2T_x$ (A_{1g} (C) in Fig. 2b). Overall, both out-of-plane vibration modes of Ti_3AlC_2 shifted due to the etching of Al and the effective exfoliation of the MXene nanoplatelets.

The morphologies of the exfoliated flakes were characterized by AFM and SEM. An AFM image of an exfoliated $Ti_3C_2T_x$ flake deposited on a silicon substrate is shown in Fig. 2c. The height of the flake is about 2.7 nm, corresponding to a monolayer sample [61]. The lateral size of the flake is about 5 μm, which is an indication that relatively large flakes have been mostly obtained due to the use of mild sonication, even though tiny fragments can also be seen that contribute less towards mechanical reinforcement. Fig. 1d is an SEM image of exfoliated $Ti_3C_2T_x$ flakes. The flakes mainly display smooth and flat surfaces, evidencing that topological undulations such as wrinkles or folds were not introduced by etching and sonication. Finally, the functional groups on the surface of $Ti_3C_2T_x$ MXene nanoplatelets were studied by FTIR spectroscopy, as shown in Figure S2 (Supporting Information). The peaks at 3428 and 1627 cm^{-1} can be assigned to the stretching vibration of hydrogen bonded hydroxyl (–OH) group and the bending vibration of C–OH bond, respectively [62].

3.2. Orientation of $Ti_3C_2T_x$ in PVA matrix

The XRD patterns of pure PVA and the $Ti_3C_2T_x$/PVA films with various loadings are shown in Fig. 3a. There is no obvious difference between the diffraction patterns of pure PVA and $Ti_3C_2T_x$/PVA

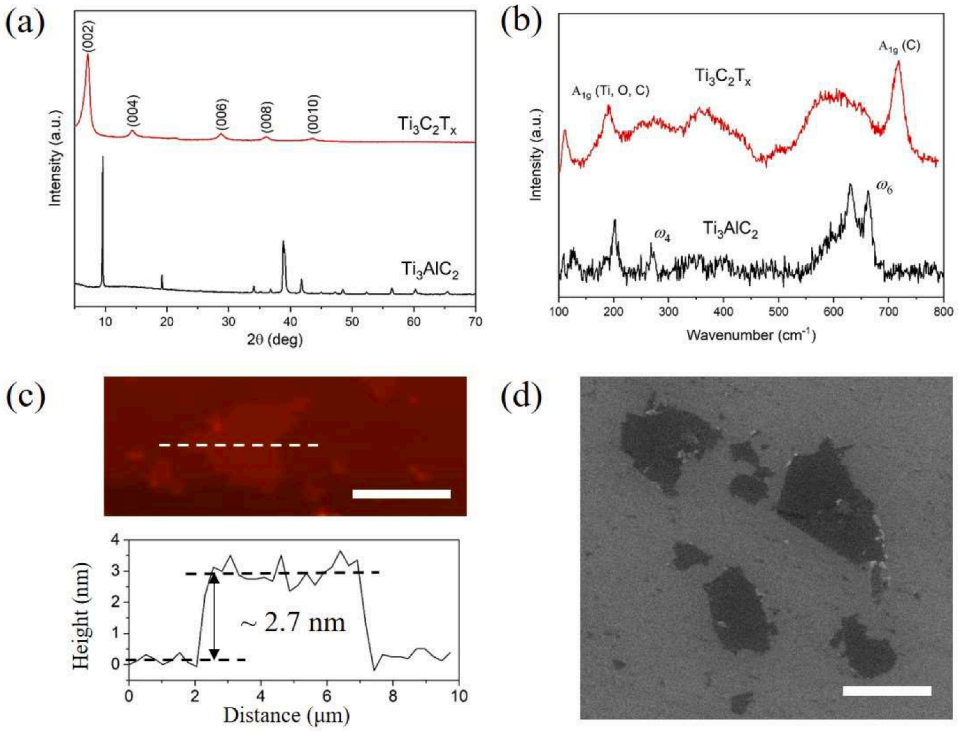

Fig. 2. (a) XRD patterns of Ti_3AlC_2 MAX and $Ti_3C_2T_x$ MXene. (b) Raman spectrum of Ti_3AlC_2 MAX and $Ti_3C_2T_x$ MXene. (c) AFM image of exfoliated $Ti_3C_2T_x$ nanosheet. Scale bar, 5 μm. (d) SEM image of exfoliated $Ti_3C_2T_x$ nanosheet. Scale bar, 2.5 μm.

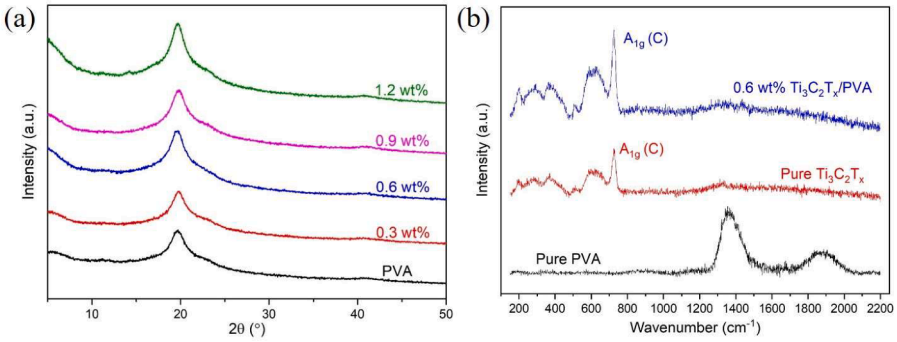

Fig. 3. (a) XRD patterns of pure PVA and $Ti_3C_2T_x$/PVA films with different filler loadings. (b) Raman spectrum of pure PVA, pure $Ti_3C_2T_x$ and 0.6 wt% $Ti_3C_2T_x$/PVA film.

composites, and all the samples show a peak at $2\theta = 19.6^{\circ}$ representing reflections from (101) plane of PVA [63]. The intensity and position of the main XRD peak was similar for all samples, an indication that degree of crystallinity, the size of PVA crystals and the orientation of PVA macromolecular chains did not change significantly with increasing $Ti_3C_2T_x$ loading. The characteristic peaks of pure $Ti_3C_2T_x$ (illustrated in Fig. 1a) are not observed in the composite films, an indication that the $Ti_3C_2T_x$ flakes were exfoliated in the PVA matrix.

Fig. 3b compares the Raman spectra of PVA, $Ti_3C_2T_x$ and $Ti_3C_2T_x$/PVA film from 150 to 2200 cm^{-1}. In contrast to the XRD patterns, the Raman spectrum of $Ti_3C_2T_x$/PVA film is dominated by the $Ti_3C_2T_x$ modes despite the low loading of the filler. $Ti_3C_2T_x$ is in resonance when the 785 nm laser is used and therefore the intensity of Raman bands is high [60]. The important work of Hu et al. [64] can serve as a useful reference towards the structural and vibrational analysis of bare Ti_3C_2 and T-terminated $Ti_3C_2T_2$ MXenes using Raman spectroscopy. The A_{1g} (C) peak of $Ti_3C_2T_x$ originating from the out-of-plane vibration of carbon atoms is intense and sharp; therefore, this peak was used for the analysis of orientation and strain-induced band shifts.

Polarized Raman spectroscopy was used to characterize the orientation of $Ti_3C_2T_x$ flakes in the PVA matrix. Polar plots of the normalized A_{1g} intensity for the 0.6 wt% $Ti_3C_2T_x$/PVA film with the laser parallel to the *z* and *x* directions are presented in Fig. 4. When the laser is parallel to the *z* direction, the intensity of the A_{1g} peak is independent of the rotation angle and is almost constant (Fig. 4a). The red solid line is the fitting curve using $I_{A1g} = 1$, indicating that $Ti_3C_2T_x$ is isotropic in the *z* axis. Therefore, the results obtained when the laser is parallel to the *x* direction will be able to describe the spatial orientation of $Ti_3C_2T_x$ in the matrix [65]. In that case, the intensity of A_{1g} peak shows a regular variation as a function of rotation angle, as illustrated in Fig. 4b. Similar results have been reported for the spatial orientation of GO in PVA using the D band [65] and GNPs in thermoplastic elastomers using the G band [66]. The following relationship was used to fit the data by using the polar coordinates of the *z* direction θ and Φ [67]

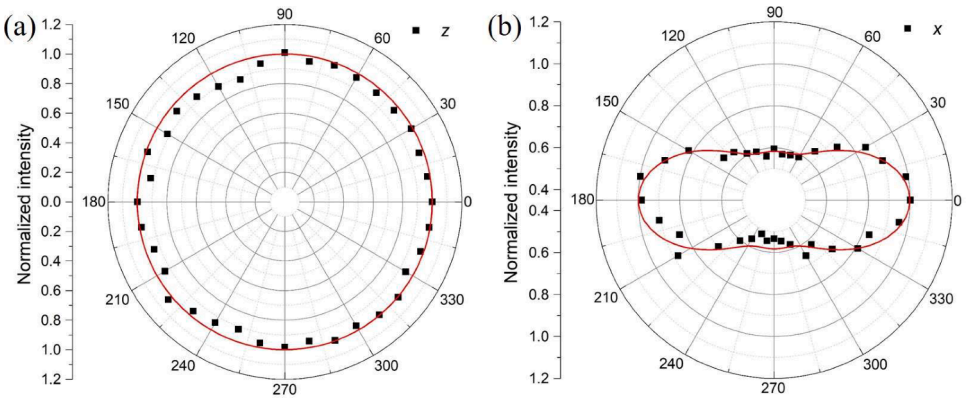

Fig. 4. Variation of the normalized intensity of A_{1g} peak with rotation angle using VV polarization when the laser is parallel to (a) *z*-axis and (b) *x-axis*, respectively. The filler loading is 0.6 wt%. The black dots represent experimental results and the red lines represent fitting results with (a) $I_{A1g} = 1$ and (b) $\langle P_2(\cos\theta)\rangle = 0.28$ and $\langle P_4(\cos\theta)\rangle = 0.30$.

$$I(\Phi) = I_o\left\{\frac{8}{15} + \langle P_2(\cos\theta)\rangle\left(-\frac{16}{21} + \frac{8}{7}\cos^2\Phi\right) + \langle P_4(\cos\theta)\rangle\left(\frac{8}{35} - \frac{8}{7}\cos^2\Phi + \cos^4\Phi\right)\right\}, \quad (1)$$

where I_o is the amplitude and $\langle P_2(\cos\theta)\rangle$ and $\langle P_4(\cos\theta)\rangle$ are fitting parameters that enable quantification of the spatial orientation of flakes in matrix [65]. These two parameters can be correlated to the Krenchel orientation factor, η_o, as

$$\eta_o = \frac{8}{15} + \frac{8}{21}\langle P_2(\cos\theta)\rangle + \frac{3}{35}\langle P_4(\cos\theta)\rangle, \quad (2)$$

where η_o is equal to 0.53 for random orientation of 2D materials within a polymer matrix and is equal to 1 for in-plane orientation [31].

For the fitting of experimental data in Fig. 4b, the parameters $\langle P_2(\cos\theta)\rangle = 0.28$ and $\langle P_4(\cos\theta)\rangle = 0.30$ were used. The results for all composites at different filler loadings are presented in Figure S4 and summarized in Table 1. There is no preferred orientation in the *z* direction, while the samples display a preferential in-plane (*x*-*y*) orientation as a result of the solution casting process. By substituting the $\langle P_2(\cos\theta)\rangle$ and $\langle P_4(\cos\theta)\rangle$ values into Eq. (2), the orientation factor (η_0) can be determined. The orientation factors are similar at different filler loadings with values varying between 0.65 and 0.67. These values are slightly lower than the in-plane orientation of the previously reported GO sheets in a PVA matrix (0.69 to 0.78), with considerably higher filler loadings [65]. Given the fact that oriented fillers along the tensile direction contribute significantly towards mechanical reinforcement, it is anticipated that the mechanical properties of the MXene nanocomposites should be considerably improved even at low filler contents.

3.3. Mechanical properties of $Ti_3C_2T_x$/PVA films

The mechanical properties of pure PVA and $Ti_3C_2T_x$/PVA nanocomposite films were characterized by tensile testing. Typical stress-strain curves of pure PVA and the 0.6 wt% $Ti_3C_2T_x$/PVA nanocomposite are presented in Fig. 5a. The elastic region of the stress-strain curves and the determination of Young's modulus is shown in Figure S5 in Supporting Information. The Young's modulus and tensile strength of the composites increased (Fig. 5b) while the elongation at break decreased with increasing $Ti_3C_2T_x$. At 0.6 wt% $Ti_3C_2T_x$, the Young's modulus of pure PVA (2.21 GPa) increased by 27% to 2.81 GPa. Beyond this concentration, the Young's modulus remained almost constant. The tensile strength improved by 24% from 68.3 to 84.9 MPa with 0.6 wt% $Ti_3C_2T_x$; however the tensile strength decreased with larger filler loading. Given that the tensile strength is more sensitive to defects and aggregation, this might be an indication that agglomerates were formed at nanocomposite loadings higher than 0.6 wt%. The SEM images taken from cryofractured samples reveal a homogeneous distribution of fillers at low contents (Fig 6a,b) which allows for efficient reinforcement, while at higher filler contents (Fig 6c,d) some aggregated regions can be seen, known to act as stress concentration points during the application of strain. It is important to notice that the MXenes appear well-wetted by the polymer matrix, ensuring that stress is transferred effectively from the matrix to the fillers. A certain degree of orientation can be also observed in all SEM images as a result of the casting process that was used to prepare the MXene nanocomposites; the degree of orientation has already been quantified through polarized Raman spectroscopy and presented in Section 3.2.

Table 1
Values of $\langle P_2(\cos\theta)\rangle$, $\langle P_4(\cos\theta)\rangle$and η_o determined for measurements where the laser beam was parallel to the *x* direction of the sample surfaces.

Samples	Filler content (wt%)	$\langle P_2(\cos\theta)\rangle$	$\langle P_4(\cos\theta)\rangle$	η_o
PVA/$Ti_3C_2T_x$	0.3	0.27	0.31	0.66
	0.6	0.28	0.30	0.67
	0.9	0.25	0.30	0.65
	1.2	0.26	0.28	0.66

The mechanical properties of polymers and their nanocomposites can be also associated with changes in the degree of crystallinity of the matrix. The degree of crystallinity of PVA and its nanocomposites, as derived from DSC curves (Figure S6) is presented in Table S1. The incorporation of $Ti_3C_2T_x$ did not change the crystallinity significantly. As a result, the changes in the mechanical properties cannot be attributed to changes in crystallinity but to the presence of the MXene nanofillers, their degree of orientation and ultimately, the formation of a strong polymer-filler interface.

3.4. Strain-induced Raman band shifts

The mechanics of filler reinforcement can be studied through the evaluation of the stress transfer mechanism at the polymer-filler interface [52]. In a previous study, the shift rate of Raman A_{1g} mode with strain was used to study the deformation and interfacial stress transfer in model Ti_3C_2 polymer nanocomposites [58]. Raman spectra with the laser beam parallel to the *z* axis were collected from $Ti_3C_2T_x$/PVA nanocomposites and the position of the A_{1g} mode was recorded as a function of strain. Fig. 7 shows the A_{1g} peak of 0.6 wt% $Ti_3C_2T_x$/PVA nanocomposite at 0 and 0.4% strain. There is a downshift of the position of the A_{1g} peak as the stress was transferred from the PVA matrix to the flake. The peaks were fitted by a single Lorentzian function (Figure S7). At 0.4% applied strain, the peak undergoes a downshift of about 1.1 cm^{-1}.

Fig. 8 shows the position of Raman A_{1g} band as a function of strain

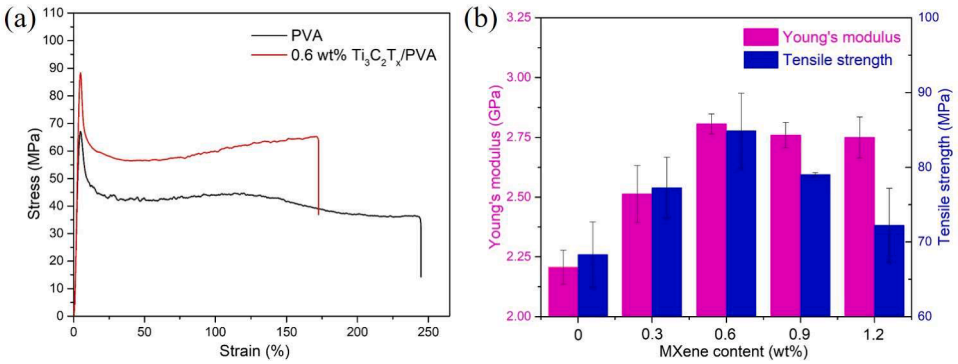

Fig. 5. (a) Stress-strain curves of pure PVA and 0.6 wt% $Ti_3C_2T_x$/PVA. (b) Young's modulus (pink bars) and tensile strength (blue bars) of pure PVA and $Ti_3C_2T_x$/PVA nanocomposites with different filler loadings (0.3, 0.6, 0.9 and 1.2 wt%).

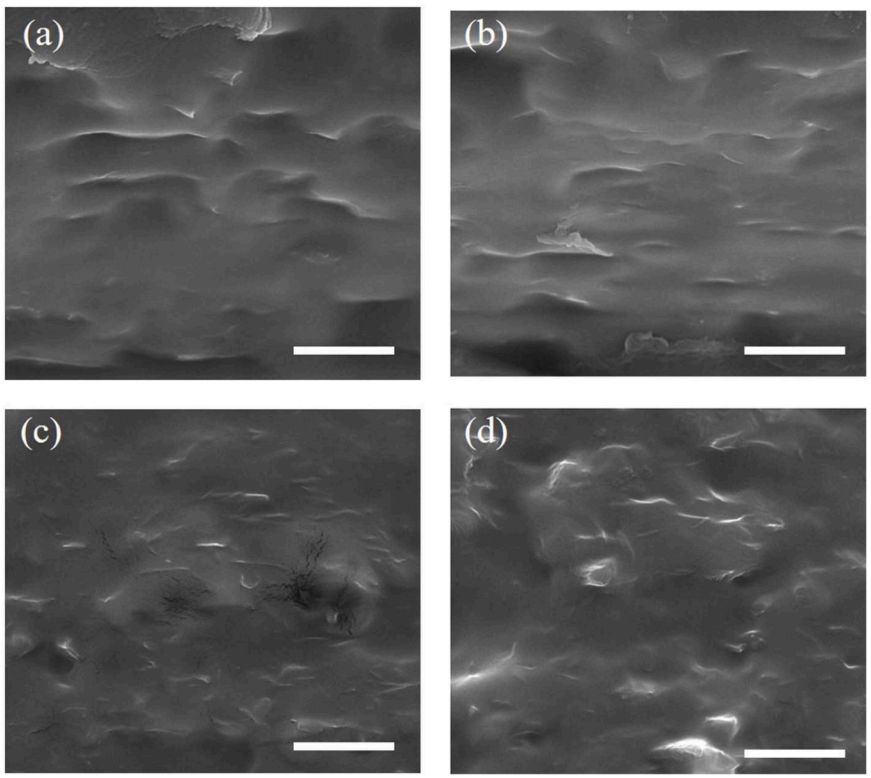

Fig. 6. SEM images of cryofractured PVA/MXene nanocomposites at (a) 0.3, (b) 0.6, (c) 0.9 and (d) 1.2 wt% filler contents. Scale bars, 2.5 μm.

measured for the $Ti_3C_2T_x$/PVA nanocomposites. There is a linear downshift in A_{1g} band position with the increase of strain until 0.45% strain for all the samples. This redshift indicates an effective stress transfer from PVA to $Ti_3C_2T_x$ flakes and the presence of a strong polymer-filler interface [68]. After that, there is no further shift in the characteristic Raman A_{1g} band which is probably induced by failure of the interface and slippage between PVA and $Ti_3C_2T_x$ [57]. The band shifts were fitted with straight lines and the slopes were obtained for all the samples. For the 0.3 wt% $Ti_3C_2T_x$/PVA nanocomposite, a slope of -2.8 ± 0.1 cm^{-1}/% was observed as shown in Fig. 8a. This value is slightly lower than the value of $Ti_3C_2T_x$ flake deposited on a PMMA beam (-3.7 cm^{-1}/%) [58]. This is reasonable as in our case the flakes were dispersed in a bulk polymer matrix and the orientation of the flakes was not perfectly parallel to the strain direction. Therefore, the flakes were not fully stretched along the in-plane direction. A slope of -2.7 ± 0.2 cm^{-1}/% was derived for the 0.6 wt% $Ti_3C_2T_x$/PVA nanocomposite as shown in Fig. 8b, which is similar to the case of the sample filled with 0.3 wt% $Ti_3C_2T_x$. When the filler content increases to 0.9 wt%, a poorer stress transfer efficiency can be deduced from the decrease of the slope of A_{1g} band position to -1.5 ± 0.1 cm^{-1}/%. The slope further decreased to -1.2 ± 0.1 cm^{-1}/% with 1.2 wt% $Ti_3C_2T_x$ filler loading. These are indications of a slight aggregation of the MXene nanoparticles, even though the loadings can be considered quite small. To avoid sample-to-sample variation, two more samples were studied for each loading and the results are illustrated in Figure S8, clearly showing that variation between samples was small. The derived slopes of Raman band shifts can be used to determine the effective Young's modulus of the filler as presented in the next section.

3.5. Micromechanics of reinforcement

The mechanics of reinforcement of a low-modulus matrix with a high-modulus filler under uniform strain can be described by the well-established modified rule of mixtures (mRoM) [69]. According to the theory, the Young's modulus of a composite, E_c, is given by

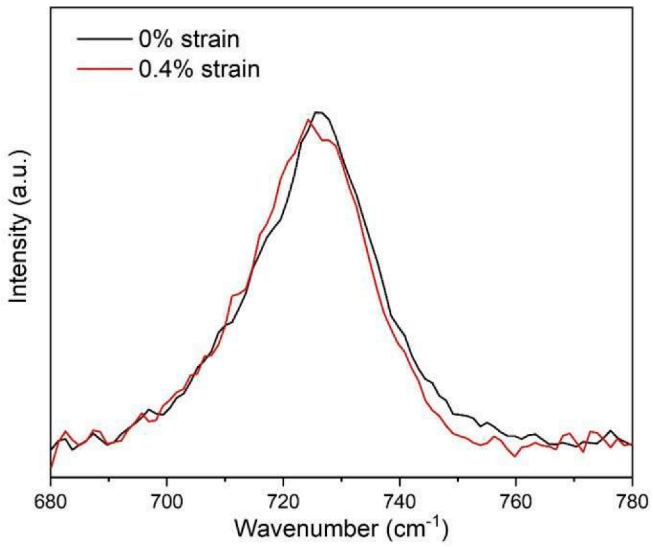

Fig. 7. Raman A_{1g} band of 0.6 wt% $Ti_3C_2T_x$/PVA nanocomposite before (0% strain) and after (0.4% strain) tensile deformation.

$$E_c = E_{eff}V_f + E_m(1 - V_f), \quad (3)$$

where E_{eff} is the effective Young's modulus of the nanofiller, E_m is the Young's modulus of the matrix, and V_f is the volume fraction of the nanofiller. The conversion of wt% to vol% is presented in Supporting Information – S9. The density of $Ti_3C_2T_x$ is 4.21 g/cm^3 and the density of PVA is 1.3 g/cm^3 [57]. The weight fractions of 0.3, 0.6, 0.9 and 1.2 wt% correspond to volume fractions of 0.09, 0.19, 0.28 and 0.37 vol%, respectively.

By substituting the volume fractions and the Young's modulus of the matrix and nanocomposites (listed in Table 2) into Eq. (3), the effective Young's modulus of $Ti_3C_2T_x$ nanoplatelets was calculated and summarized in Table 2. The E_{eff} of $Ti_3C_2T_x$ is about 342.9 and 318.0 GPa for 0.3 wt% and 0.6 wt% loadings, respectively, and reduces to 199.8 GPa at 0.9 wt% and 149.1 GPa at 1.2 wt%. The dependence of E_c upon V_f for the nanocomposites is shown in Figure S9. There is an approximately linear increase in composite modulus with volume fraction until 0.6 wt%. From the initial slope of the curve, the value of E_{eff} for $Ti_3C_2T_x$ was determined to be 314.4 GPa, which is close to the values determined using Eq. (3) for the nanocomposites with 0.3 and 0.6 wt% filler content.

The effective Young's modulus of MXene flakes can also be estimated independently from the Raman band shift rates upon strain (E_R). The shift rates of A_{1g} band derived in Section 3.4 can be used to determine the value of E_R as

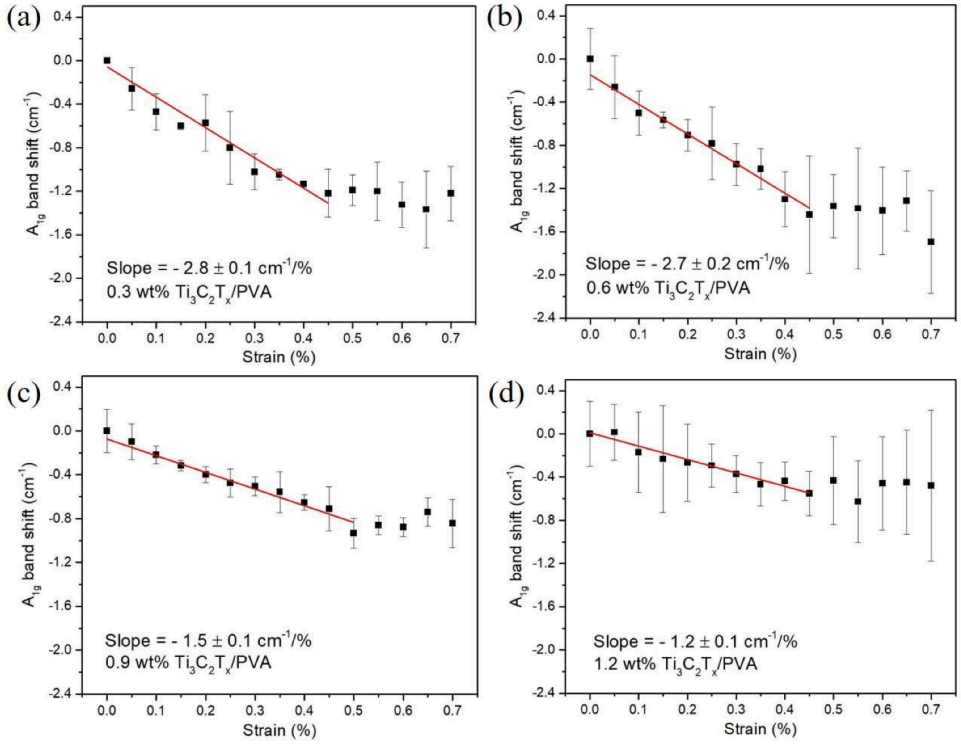

Fig. 8. Strain-induced Raman A_{1g} band shifts of $Ti_3C_2T_x$/PVA nanocomposites at (a) 0.3, (b) 0.6, (c) 0.9 and (d) 1.2 wt% filler contents.

Table 2
Mechanical properties of PVA/$Ti_3C_2T_x$ nanocomposites and filler modulus determined from mechanical testing and Raman band shifts.

Samples	Filler content (wt%, vol%)	Young's modulus (GPa)	E_{eff} (GPa) (Mechanical)	η_l	$d\omega_{A1g}/d\varepsilon$ (cm^{-1}/%)	E_R (GPa) (Raman)
PVA	0, 0	2.21 ± 0.07	–	–	–	–
PVA/$Ti_3C_2T_x$	0.3, 0.09	2.51 ± 0.12	342.9	1	2.7 ± 0.1	366.3
	0.6, 0.19	2.81 ± 0.04	318.0	0.95	2.7 ± 0.1	366.3
	0.9, 0.28	2.76 ± 0.05	199.8	0.61	1.5 ± 0.1	203.5
	1.2, 0.37	2.75 ± 0.09	149.1	0.45	1.3 ± 0.1	176.4

$$E_R = \frac{d\omega_{A_{1g}}}{d\varepsilon}\frac{E_f}{\left(d\omega_{A_{1g}}/d\varepsilon\right)_{ref}}\text{GPa}, \quad (4)$$

where $d\omega_{A1g}/d\varepsilon$ is the shift rate of $Ti_3C_2T_x$ Raman A_{1g} mode with strain, the reference shift rate value is taken as -3.7 $cm^{-1}/\%$, and E_f is the intrinsic Young's modulus of monolayer $Ti_3C_2T_x$. Here, the E_f value of 502 GPa (Ti_3C_2) was used [43], as it has been shown that the Young's modulus of $Ti_3C_2T_x$ is similar with the value of Ti_3C_2 [44]. The values of the effective Young's modulus of $Ti_3C_2T_x$ as determined from Raman band shifts are listed in Table 2. It can be seen that E_R is generally higher than E_{eff}. Similar behaviour has been observed in a number of polymers reinforced by GNPs and can be attributed to a higher degree of orientation and possibly a higher aspect ratio of the individual flakes that have been studied by Raman spectroscopy [52].

The determination of the effective Young's modulus allows the mechanical reinforcing efficiency to be evaluated. If we take the effect of orientation and finite length of flakes into account, the effective Young's modulus can be given as [57]

$$E_{eff} = \eta_l \eta_o E_f, \quad (5)$$

where E_f is the Young's modulus of the flake, η_o is the Krenchel orientation factor that was calculated in Section 3.2 and η_l is the length factor that takes values between 0 (for no stress transfer) and 1 (for perfect stress transfer). The length factor reflects the stress transfer efficiency from the matrix to the filler which is not only dependent on the shape of the filler but also on the interfacial strength between the filler and the matrix; therefore its determination is critical towards understanding the micromechanics of reinforcement [52]. If we use the effective Young's modulus from mechanical testing and the orientation factor from Raman spectra (Table 1), the length factor can be calculated. The results are summarized in Table 2. It can be seen that the length factor is close to 1 at 0.3 and 0.6 wt% filler loadings, indicating effective stress transfer from the matrix to the MXenes at low loadings. With further increase in filler loading, the length factor was degraded, dropping to 0.61 at 0.9 wt % and 0.45 at 1.2 wt%. This is consistent with the stress-induced Raman band shifts as stated above. The slight aggregation of the MXene nanoparticles at 0.9 and 1.2 wt% leads to a deterioration of the stress transfer from the matrix to the filler which is also reflected in the reduction of the length factor.

4. Conclusions

The introduction of $Ti_3C_2T_x$ flakes in a PVA matrix leads to an improvement of mechanical properties. A new insight into the micromechanics of reinforcement of $Ti_3C_2T_x$ MXene within the PVA matrix was provided using Raman spectroscopy. Specifically, the spatial distribution of $Ti_3C_2T_x$ in PVA was characterized by polarized Raman spectroscopy and the Krenchel orientation factor was determined quantitatively. The results revealed that nanoplatelets displayed a certain degree of in-plane orientation, which allows for effective reinforcement along the tensile direction. The interfacial interactions were evaluated by strain-induced Raman band shifts for all nanocomposites under study. This allowed the calculation of the effective Young's modulus of $Ti_3C_2T_x$ which showed good agreement with the values derived from mechanical testing. The effective Young's modulus of MXene nanoplatelets was in the order of 300 GPa at low filler contents, revealing the great potential of the filler towards mechanical reinforcement of bulk polymers in a number of applications, once MXene scalability and fabrication issues are resolved. Lastly, this work revealed once again the wealth of information that can be exported through the use of Raman spectroscopy in strong resonance systems such as 2D materials- reinforced polymer nanocomposites.

CRediT authorship contribution statement

Ming Dong: Conceptualization, Data curation, Formal analysis, Investigation, Validation, Visualization, Writing – original draft, Writing – review & editing. **Yi Hu:** Data curation, Investigation. **Han Zhang:** Writing – review & editing. **Emiliano Bilotti:** Writing – review & editing. **Nicola Pugno:** Writing – review & editing. **David Dunstan:** Supervision, Writing – review & editing. **Dimitrios G. Papageorgiou:** Funding acquisition, Project administration, Supervision, Validation, Writing – original draft, Writing – review & editing.

Declaration of Competing Interest

The authors declare that they have no known competing financial interests or personal relationships that could have appeared to influence the work reported in this paper.

Data availability

Data will be made available on request.

Acknowledgment

M. Dong acknowledges support from the China Scholarship Council (CSC). The authors acknowledge the support from "Graphene Core 3″ GA: 881603 which is implemented under the EU-Horizon 2020 Research & Innovation Actions (RIA) and is financially supported by EU-financed parts of the Graphene Flagship.

Supplementary materials

Supplementary material associated with this article can be found, in the online version, at doi:10.1016/j.jcomc.2023.100427.

References

[1] K.S. Novoselov, A.K. Geim, S.V. Morozov, D. Jiang, Y. Zhang, S.V. Dubonos, et al., Electric field effect in atomically thin carbon films, Science 306 (2004) 666–669.
[2] Q.H. Weng, X.B. Wang, X. Wang, Y. Bando, D. Golberg, Functionalized hexagonal boron nitride nanomaterials: emerging properties and applications, Chem. Soc. Rev. 45 (2016) 3989–4012.
[3] X. Li, H.W. Zhu, Two-dimensional MoS_2: properties, preparation, and applications, J. Materiom. 1 (2015) 33–44.
[4] M. Naguib, V.N. Mochalin, M.W. Barsoum, Y. Gogotsi, 25th anniversary article: MXenes: a new family of two-dimensional materials, Adv. Mater. 26 (2014) 992–1005.
[5] M.T. Zhao, Q.P. Lu, Q.L. Ma, H. Zhang, Two-dimensional metal-organic framework nanosheets, Small Methods 1 (2017) 1600030.
[6] A.C. Ferrari, F. Bonaccorso, V. Fal'ko, K.S. Novoselov, S. Roche, P. Boggild, et al., Science and technology roadmap for graphene, related two-dimensional crystals, and hybrid systems, Nanoscale 7 (2015) 4598–4810.
[7] A.V. Mohammadi, J. Rosen, Y. Gogotsi, The world of two-dimensional carbides and nitrides (MXenes), Science 372 (2021) eabf1581.
[8] M. Shekhirev, C.E. Shuck, A. Sarycheva, Y. Gogotsi, Characterization of MXenes at every step, from their precursors to single flakes and assembled films, Prog. Mater. Sci. 120 (2021) 31.
[9] M. Naguib, M. Kurtoglu, V. Presser, J. Lu, J.J. Niu, M. Heon, et al., Two-dimensional nanocrystals produced by exfoliation of Ti_3AlC_2, Adv. Mater. 23 (2011) 4248–4253.
[10] M. Naguib, M.W. Barsoum, Y. Gogotsi, Ten years of progress in the synthesis and development of MXenes, Adv. Mater. 33 (2021) 10.
[11] T.L. Tan, H.M. Jin, M.B. Sullivan, B. Anasori, Y. Gogotsi, High-throughput survey of ordering configurations in MXene alloys across compositions and temperatures, ACS Nano 11 (2017) 4407–4418.
[12] M. Khazaei, A. Ranjbar, M. Arai, T. Sasaki, S. Yunoki, Electronic properties and applications of MXenes: a theoretical review, J. Mater. Chem. C 5 (2017) 2488–2503.
[13] J.Z. Zhang, N. Kong, S. Uzun, A. Levitt, S. Seyedin, P.A. Lynch, et al., Scalable manufacturing of free-standing, strong $Ti_3C_2T_x$ MXene films with outstanding conductivity, Adv. Mater. 32 (2020) 9.
[14] A. Lipatov, A. Goad, M.J. Loes, N.S. Vorobeva, J. Abourahma, Y. Gogotsi, et al., High electrical conductivity and breakdown current density of individual monolayer $Ti_3C_2T_x$ MXene flakes, Matter 4 (2021) 1413–1427.

[15] M.R. Lukatskaya, S. Kota, Z.F. Lin, M.Q. Zhao, N. Shpigel, M.D. Levi, et al., Ultra-high-rate pseudocapacitive energy storage in two-dimensional transition metal carbides, Nat. Energy 2 (2017) 6.

[16] B. Anasori, M.R. Lukatskaya, Y. Gogotsi, 2D metal carbides and nitrides (MXenes) for energy storage, Nat. Rev. Mater. 2 (2017) 17.

[17] N.K. Chaudhari, H. Jin, B. Kim, D.S. Baek, S.H. Joo, K. Lee, MXene: an emerging two-dimensional material for future energy conversion and storage applications, J. Mater. Chem. A 5 (2017) 24564–24579.

[18] H. Wang, Y. Wu, X.Z. Yuan, G.M. Zeng, J. Zhou, X. Wang, et al., Clay-inspired MXene-based electrochemical devices and photo-electrocatalyst: state-of-the-art progresses and challenges, Adv. Mater. 30 (2018) 28.

[19] A. Shahzad, K. Rasool, M. Nawaz, W. Miran, J. Jang, M. Moztahida, et al., Heterostructural $TiO_2/Ti_3C_2T_x$ (MXene) for photocatalytic degradation of antiepileptic drug carbamazepine, Chem. Eng. J. 349 (2018) 748–755.

[20] F. Shahzad, M. Alhabeb, C.B. Hatter, B. Anasori, S.M. Hong, C.M. Koo, et al., Electromagnetic interference shielding with 2D transition metal carbides (MXenes), Science 353 (2016) 1137–1140.

[21] A. Iqbal, F. Shahzad, K. Hantanasirisakul, M.K. Kim, J. Kwon, J. Hong, et al., Anomalous absorption of electromagnetic waves by 2D transition metal carbonitride Ti_3CNT_x (MXene), Science 369 (2020) 446–450.

[22] T.Y. Zhang, H. Wang, J. Tong, J. Zhang, X. Wang, Y. Zeng, High-efficiency ultraviolet shielding and high transparency of $Ti_3C_2T_x$ MXene/poly(vinyl alcohol) nanocomposite films, Compos. Commun. 33 (2022), 101235.

[23] Y.Y. Pei, X.L. Zhang, Z.Y. Hui, J.Y. Zhou, X. Huang, G.Z. Sun, et al., $Ti_3C_2T_X$ MXene for sensing applications: recent progress, design principles, and future perspectives, ACS Nano 15 (2021) 3996–4017.

[24] D.H. Ho, Y.Y. Choi, S.B. Jo, J.M. Myoung, J.H. Cho, Sensing with mxenes: progress and prospects, Adv. Mater. 33 (2021) 29.

[25] K. Hantanasirisakul, Y. Gogotsi, Electronic and optical properties of 2D transition metal carbides and nitrides (MXenes), Adv. Mater. 30 (2018) 1804779.

[26] A. Ahmed, S. Sharma, B. Adak, M.M. Hossain, A.M. LaChance, S. Mukhopadhyay, et al., Two-dimensional MXenes: new frontier of wearable and flexible electronics, InfoMat 4 (2022) 28.

[27] S. Chertopalov, V.N. Mochalin, Environment-sensitive photoresponse of spontaneously partially oxidized Ti_3C_2 MXene thin films, ACS Nano 12 (2018) 6109–6116.

[28] X.X. Zhan, C. Si, J. Zhou, Z.M. Sun, MXene and MXene-based composites: synthesis, properties and environment-related applications, Nanoscale Horiz. 5 (2020) 235–258.

[29] H. Lin, Y. Chen, J.L. Shi, Insights into 2D MXenes for versatile biomedical applications: current advances and challenges ahead, Adv. Sci. 5 (2018) 1800518.

[30] M. Soleymaniha, M.A. Shahbazi, A.R. Rafieerad, A. Maleki, A. Amiri, Promoting role of MXene nanosheets in biomedical sciences: therapeutic and biosensing innovations, Adv. Healthc. Mater. 8 (2019) 26.

[31] D.G. Papageorgiou, Z.L. Li, M.F. Liu, I.A. Kinloch, R.J. Young, Mechanisms of mechanical reinforcement by graphene and carbon nanotubes in polymer nanocomposites, Nanoscale 12 (2020) 2228–2267.

[32] X. Shen, Q.B. Zheng, J.K. Kim, Rational design of two-dimensional nanofillers for polymer nanocomposites toward multifunctional applications, Prog. Mater. Sci. 115 (2021) 65.

[33] M. Dong, H. Zhang, L. Tzounis, G. Santagiuliana, E. Bilotti, D.G. Papageorgiou, Multifunctional epoxy nanocomposites reinforced by two-dimensional materials: a review, Carbon 185 (2021) 57–81.

[34] H. Riazi, S.K. Nemani, M.C. Grady, B. Anasori, M. Soroush, Ti_3C_2 MXene-polymer nanocomposites and their applications, J. Mater. Chem. A 9 (2021) 8051–8098.

[35] K.L. Gong, K.Q. Zhou, X.D. Qian, C.L. Shi, B. Yu, MXene as emerging nanofillers for high-performance polymer composites: a review, Compos. B 217 (2021) 40.

[36] L.F. Gao, C. Li, W.C. Huang, S. Mei, H. Lin, Q. Ou, et al., MXene/polymer membranes: synthesis, properties, and emerging applications, Chem. Mater. 32 (2020) 1703–1747.

[37] Z. Ling, C.E. Ren, M.Q. Zhao, J. Yang, J.M. Giammarco, J.S. Qiu, et al., Flexible and conductive MXene films and nanocomposites with high capacitance, Proc. Natl. Acad. Sci. U.S.A. 111 (2014) 16676–16681.

[38] H. Yan, M. Cai, W. Li, X.Q. Fan, M.H. Zhu, Amino-functionalized $Ti_3C_2T_x$ with anti-corrosive/wear function for waterborne epoxy coating, J. Mater. Sci. Technol. 54 (2020) 144–159.

[39] R.H. Sun, H.B. Zhang, J. Liu, X. Xie, R. Yang, Y. Li, et al., Highly conductive transition metal carbide/carbonitride(MXene)@polystyrene nanocomposites fabricated by electrostatic assembly for highly efficient electromagnetic interference shielding, Adv. Funct. Mater. 27 (2017) 11.

[40] M. Malaki, R.S. Varma, Mechanotribological aspects of MXene-reinforced nanocomposites, Adv. Mater. 32 (2020) 20.

[41] A. Lipatov, H.D. Lu, M. Alhabeb, B. Anasori, A. Gruverman, Y. Gogotsi, et al., Elastic properties of 2D $Ti_3C_2T_x$ MXene monolayers and bilayers, Sci. Adv. 4 (2018) 7.

[42] A. Lipatov, M. Alhabeb, H.D. Lu, S.S. Zhao, M.J. Loes, N.S. Vorobeva, et al., Electrical and elastic properties of individual single-layer $Nb_4C_3T_x$ MXene flakes, Adv. Electron. Mater. 6 (2020) 10.

[43] V.N. Borysiuk, V.N. Mochalin, Y. Gogotsi, Molecular dynamic study of the mechanical properties of two-dimensional titanium carbides $Ti_{n+1}C_n$ (MXenes), Nanotechnology 26 (2015) 10.

[44] T. Hu, J. Yang, W. Li, X. Wang, C.M. Li, Quantifying the rigidity of 2D carbides (MXenes), Phys. Chem. Chem. Phys. 22 (2020) 2115–2121.

[45] L. Liu, G. Ying, D. Wen, K. Zhang, C. Hu, Y. Zheng, et al., Aqueous solution-processed MXene ($Ti_3C_2T_x$) for non-hydrophilic epoxy resin-based composites with enhanced mechanical and physical properties, Mater. Des. 197 (2021), 109276.

[46] R. Wazalwar, M. Tripathi, A.M. Raichur, Curing behavior and mechanical properties of tetra-functional epoxy reinforced with polyethyleneimine-functionalized MXene, ACS Appl. Polym. Mater. 4 (2022) 2573–2584.

[47] H. Zhang, L.B. Wang, Q. Chen, P. Li, A.G. Zhou, X.X. Cao, et al., Preparation, mechanical and anti-friction performance of MXene/polymer composites, Mater. Des. 92 (2016) 682–689.

[48] X.X. Sheng, Y.F. Zhao, L. Zhang, X. Lu, Properties of two-dimensional Ti_3C_2 MXene/thermoplastic polyurethane nanocomposites with effective reinforcement via melt blending, Compos. Sci. Technol. 181 (2019) 107710.

[49] W.Q. Zhi, S.L. Xiang, R.J. Bian, R.Z. Lin, K.H. Wu, T.W. Wang, et al., Study of MXene-filled polyurethane nanocomposites prepared via an emulsion method, Compos. Sci. Technol. 168 (2018) 404–411.

[50] J.Q. Luo, S. Zhao, H.B. Zhang, Z.M. Deng, L.L. Li, Z.Z. Yu, Flexible, stretchable and electrically conductive MXene/natural rubber nanocomposite films for efficient electromagnetic interference shielding, Compos. Sci. Technol. 182 (8) (2019).

[51] D.G. Papageorgiou, I.A. Kinloch, R.J. Young, Mechanical properties of graphene and graphene-based nanocomposites, Prog. Mater. Sci. 90 (2017) 75–127.

[52] R.J. Young, M.F. Liu, I.A. Kinloch, S.H. Li, X. Zhao, C. Valles, et al., The mechanics of reinforcement of polymers by graphene nanoplatelets, Compos. Sci. Technol. 154 (2018) 110–116.

[53] T.M.G. Mohiuddin, A. Lombardo, R.R. Nair, A. Bonetti, G. Savini, R. Jalil, et al., Uniaxial strain in graphene by Raman spectroscopy: G peak splitting, Gruneisen parameters, and sample orientation, Phys. Rev. B 79 (2009) 205433.

[54] L.B. Deng, S.J. Eichhorn, C.C. Kao, R.J. Young, The effective young's modulus of carbon nanotubes in composites, ACS Appl. Mater. Interfaces 3 (2011) 433–440.

[55] Z.L. Li, R.J. Young, I.A. Kinloch, Interfacial stress transfer in graphene oxide nanocomposites, ACS Appl. Mater. Interfaces 5 (2013) 456–463.

[56] F. Wang, S.H. Li, M.A. Bissett, I.A. Kinloch, Z.L. Li, R.J. Young, Strain engineering in monolayer WS_2 and WS_2 nanocomposites, 2D Mater. 7 (2020), 045022.

[57] W.M. Wang, Z.L. Li, A.J. Marsden, M.A. Bissett, R.J. Young, Mechanisms of reinforcement of PVA-Based nanocomposites by hBN nanosheets, Compos. Sci. Technol. 218 (2022) 109131.

[58] M. Liu, Y. Zhuo, A. Sarycheva, Y. Gogotsi, M.A. Bissett, R.J. Young, et al., Deformation of and interfacial stress transfer in Ti_3C_2 MXene—polymer composites, ACS Appl. Mater. Interfaces 14 (2022) 10681–10690.

[59] M. Alhabeb, K. Maleski, B. Anasori, P. Lelyukh, L. Clark, S. Sin, et al., Guidelines for synthesis and processing of two-dimensional titanium carbide ($Ti_3C_2T_X$ MXene), Chem. Mater. 29 (2017) 7633–7644.

[60] A. Sarycheva, Y. Gogotsi, Raman spectroscopy analysis of the structure and surface chemistry of $Ti_3C_2T_x$ MXene, Chem. Mater. 32 (2020) 3480–3488.

[61] A. Lipatov, M. Alhabeb, M.R. Lukatskaya, A. Boson, Y. Gogotsi, A. Sinitskii, Effect of synthesis on quality, electronic properties and environmental stability of individual monolayer Ti_3C_2 MXene flakes, Adv. Electron. Mater. 2 (2016) 1600255.

[62] N.U. Kiran, A.B. Deore, M.A. More, D.J. Late, C.S. Rout, P. Mane, et al., Comparative study of cold electron emission from 2D $Ti_3C_2T_x$ MXene nanosheets with respect to its precursor Ti_3SiC_2 MAX phase, ACS Appl. Electron. Mater. 4 (2022) 2656–2666.

[63] S. Gupta, A.K. Pramanik, A. Kailath, T. Mishra, A. Guha, S. Nayar, et al., Composition dependent structural modulations in transparent poly(vinyl alcohol) hydrogels, Colloids Surf. B 74 (2009) 186–190.

[64] T. Hu, J. Wang, H. Zhang, Z. Li, M. Hu, X. Wang, Vibrational properties of Ti_3C_2 and $Ti_3C_2T_2$ (T = O, F, OH) monosheets by first-principles calculations: a comparative study, Phys. Chem. Chem. Phys. 17 (2015) 9997–10003.

[65] Z.L. Li, R.J. Young, N.R. Wilson, I.A. Kinloch, C. Valles, Z. Li, Effect of the orientation of graphene-based nanoplatelets upon the Young's modulus of nanocomposites, Compos. Sci. Technol. 123 (2016) 125–133.

[66] M.F. Liu, D.G. Papageorgiou, S.H. Li, K.L. Lin, I.A. Kinloch, R.J. Young, Micromechanics of reinforcement of a graphene-based thermoplastic elastomer nanocomposite, Compos. A 110 (2018) 84–92.

[67] Z.L. Li, R.J. Young, I.A. Kinloch, N.R. Wilson, A.J. Marsden, A.P.A. Raju, Quantitative determination of the spatial orientation of graphene by polarized Raman spectroscopy, Carbon 88 (2015) 215–224.

[68] D.G. Papageorgiou, I.A. Kinloch, R.J. Young, Hybrid multifunctional graphene/glass-fibre polypropylene composites, Compos. Sci. Technol. 137 (2016) 44–51.

[69] R.J. Young, P.A. Lovell, Introduction to Polymers, 3rd Edition, Taylor & Francis, 2011.

Supporting information: Micromechanics of $Ti_3C_2T_x$ MXene reinforced poly(vinyl alcohol) nanocomposites

Ming Dong[1], Yi Hu[2,3], Han Zhang[2], Emiliano Bilotti[2,4], Nicola Pugno[2,5], David Dunstan[1], Dimitrios G. Papageorgiou[2*]

[1] School of Physical and Chemical Sciences, Queen Mary University of London, London E1 4NS, United Kingdom
[2] School of Engineering and Materials Science, Queen Mary University of London, London E1 4NS, United Kingdom
[3] School of Mechanical Engineering, Northwestern Polytechnical University, Xi'an, 710072, PR China
[4] Department of Aeronautics, Imperial College London, South Kensington Campus, SW7 2AZ London, United Kingdom
[5] Laboratory for Bioinspired, Bionic, Nano, Meta Materials & Mechanics, Department for Civil, Environmental and Mechanical Engineering, University of Trento, Via Mesiano 77, Trento, 38123, Italy

**Corresponding author's email: m.dong@qmul.ac.uk, d.papageorgiou@qmul.ac.uk*

Contents:

S10. Dependence of the Young's modulus of the nanocomposite upon filler loading

S1. Pure MXene film prepared by vacuum filtration

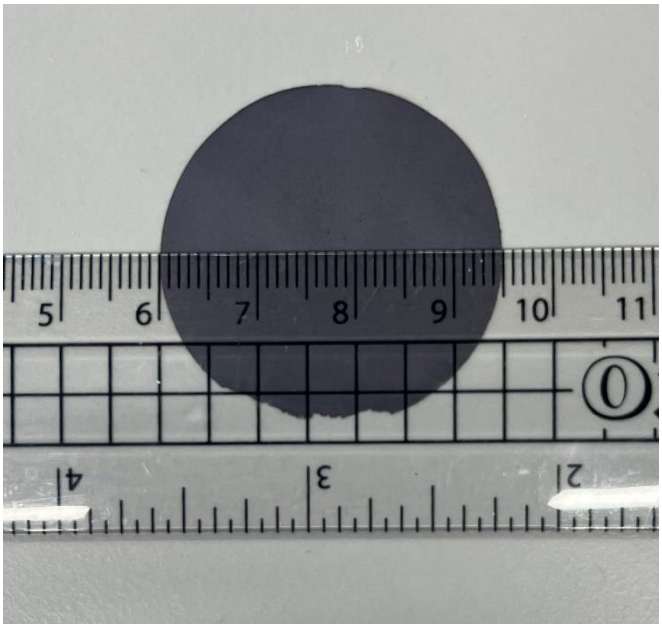

Figure S1. Photograph of pure MXene film prepared by vacuum filtration. About 7 ml MXene suspension was used for filtration and the weight of the film was about 21 mg.

S2. FTIR spectroscopy of $Ti_3C_2T_x$ MXene

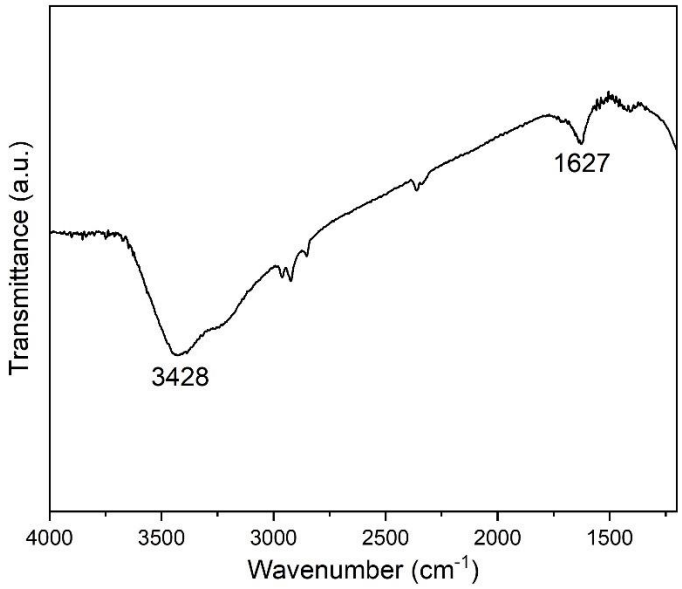

Figure S2. FTIR spectrum of $Ti_3C_2T_x$ MXene.

S3. Polarized Raman spectroscopy for orientation analysis

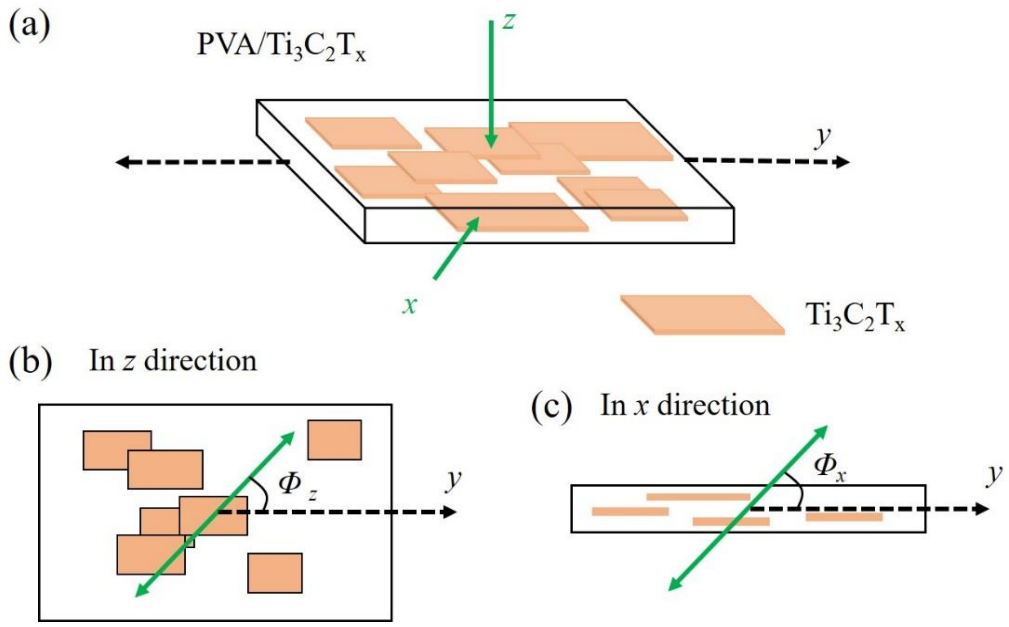

Figure S3. (a) Scheme of polarized Raman spectroscopy for orientation study of $Ti_3C_2T_x$/PVA nanocomposites. (b) The laser is parallel to the *z* direction. (c) The laser is parallel to the *x* direction.

S4. Orientation of $Ti_3C_2T_x$ in PVA matrix

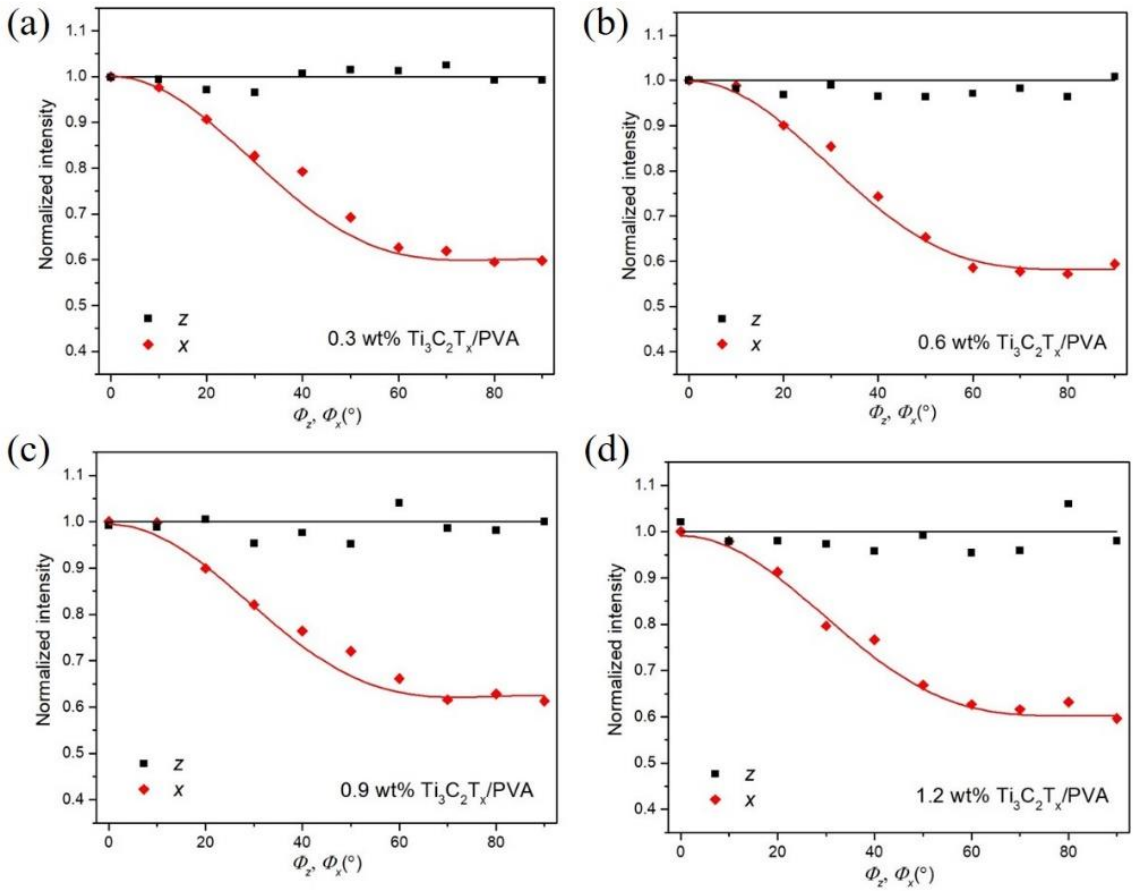

Figure S4. Normalized intensity of A_{1g} peak with rotation for $Ti_3C_2T_x$/PVA film with (a) 0.3, (b) 0.6, (c) 0.9 and (d) 1.2 wt% filler loading, respectively. The dots represent experimental results and the lines represent fitting results.

S5. Estimation of Young's modulus

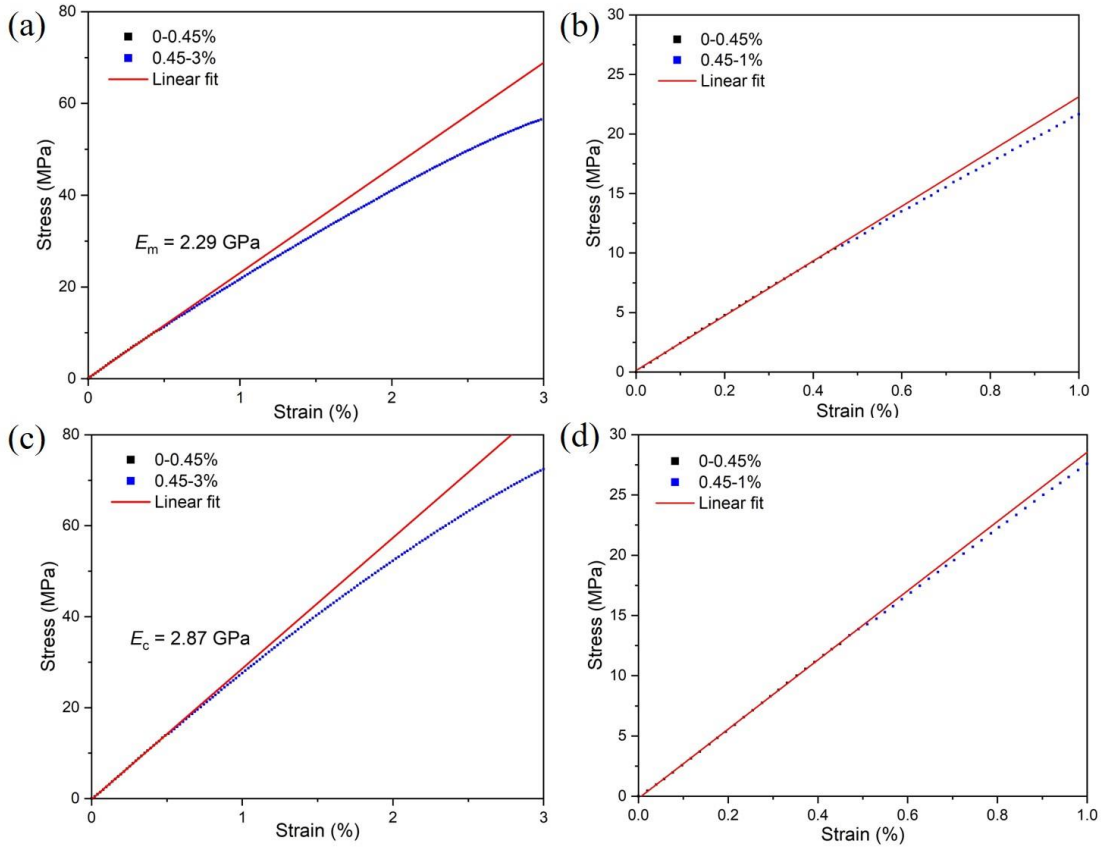

Figure S5. Stress-strain curves of PVA in the strain range between (a) 0-3% and (b) 0-1%, and of the 0.6 wt% $Ti_3C_2T_x$/PVA sample in the strain range between (c) 0-3% and (d) 0-1%.

Figure S6 shows typical stress-strain curves from which the Young's modulus is determined. For the applied strain from 0 to 0.45%, the curve is linear and the slope of the curve is used to determine the Young's modulus. The Young's modulus is 2.29 GPa for PVA and 2.87 GPa for 0.6 wt% $Ti_3C_2T_x$/PVA. With the increase of strain, there is a deviation of the experimental values from the linear fit. This indicates that chain slippage occurs.

S6. DSC analysis of PVA and $Ti_3C_2T_x$/PVA films

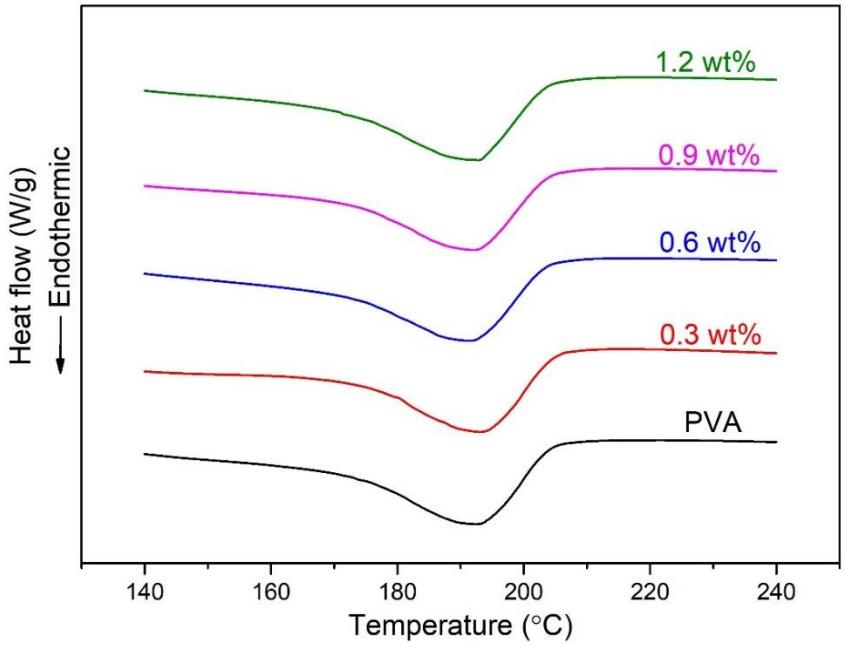

Figure S6. Melting peaks of pure PVA and $Ti_3C_2T_x$/PVA films with different filler loadings (0.3, 0.6, 0.9, 1.2 wt%).

The degree of crystallinity (f_c) was determined using the following equation

$$f_c = \frac{\Delta H_m}{\Delta H_0}, \quad \text{(S1)}$$

where ΔH_m is the measured melting enthalpy (from DSC) and ΔH_0 is the enthalpy of pure PVA crystal (138.6 J g^{-1}) [1].

Table S1. DSC results of pure PVA and $Ti_3C_2T_x$/PVA films. (T_m, melting temperature)

Samples	**Filler content (wt%)**	T_m **(°C)**	ΔH_m **(J/g)**	**Degree of Crystallinity**
PVA	0	192.8	30.9	22.3%
PVA/$Ti_3C_2T_x$	0.3	193.3	30.3	21.9%
	0.6	191.8	30.1	21.7%
	0.9	192.5	29.1	21.0%
	1.2	193.0	30.2	21.8%

S7. Fitting of Raman A_{1g} peak of MXene

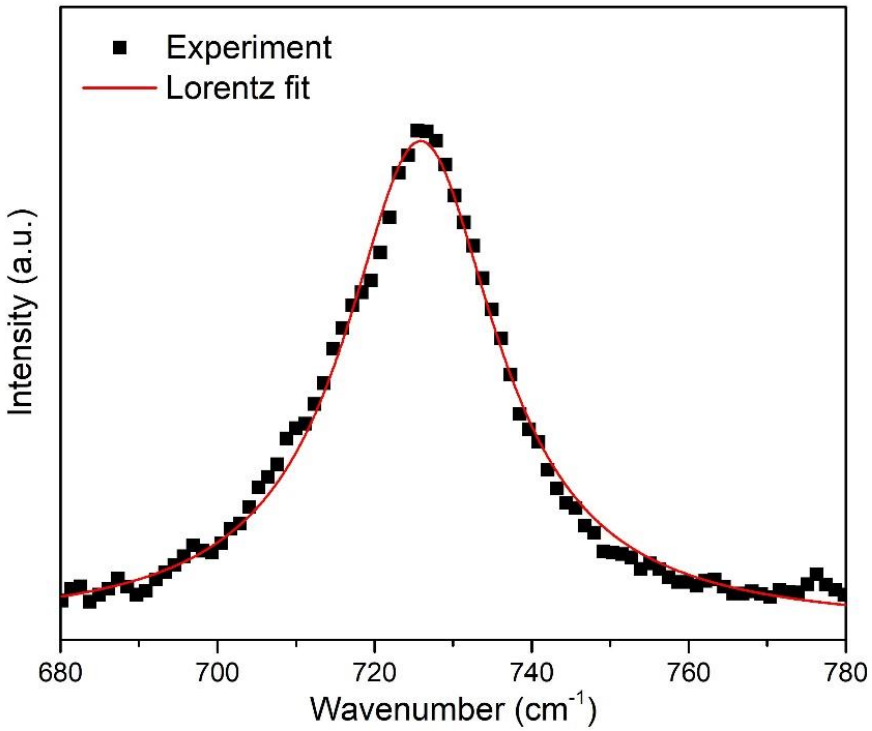

Figure S7. Lorentz fit of the Raman A_{1g} band of $Ti_3C_2T_x$.

S8. Strain-induced Raman band shifts

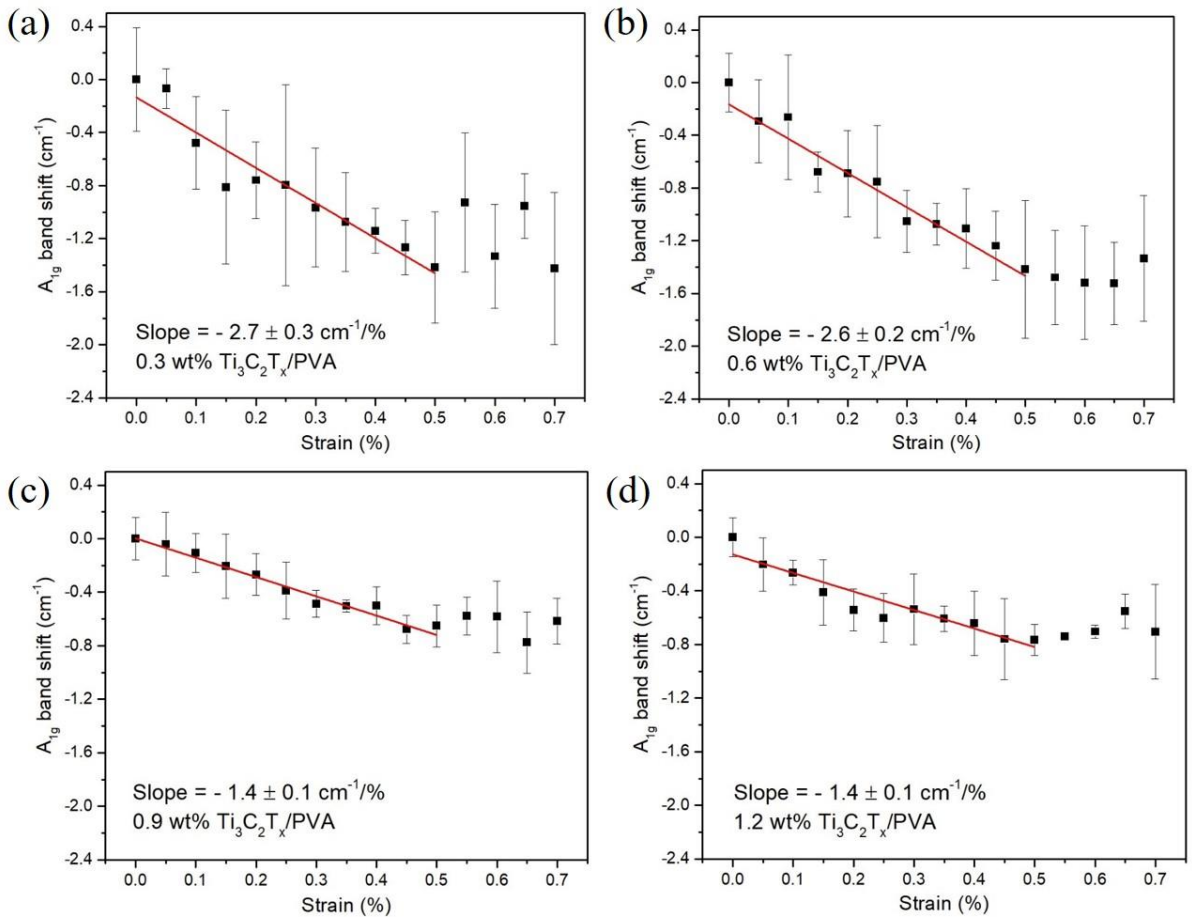

Figure S8. Strain-induced Raman A_{1g} band shifts of $Ti_3C_2T_x$/PVA nanocomposites with (a) 0.3, (b) 0.6, (c) 0.9 and (d) 1.2 wt% filler loadings.

S9. Conversion of weight content to volume content

In this study, the nanocomposites were prepared in terms of the weight percentage of PVA and $Ti_3C_2T_x$. Therefore, it is necessary to convert the weight percentage (wt%) to volume percentage (vol%). The following equation is used for the conversion [2]

$$V_f = \frac{w_f \rho_m}{w_f \rho_m + (1 - w_f)\rho_f}, \quad \text{(s1)}$$

where V_f and w_f are the volume fraction and the weight fraction of the filler, and ρ_m and ρ_f are the density of the matrix and the filler, respectively. The density of $Ti_3C_2T_x$ is 4.21 g/cm^3 and the density of PVA is 1.3 g/cm^3 [3]. Then the weight fractions of 0.3, 0.6, 0.9 and 1.2 wt% were converted to volume fractions of 0.09, 0.19, 0.28 and 0.37 vol%, respectively.

S10. Dependence of the Young's modulus of the nanocomposite upon filler loading

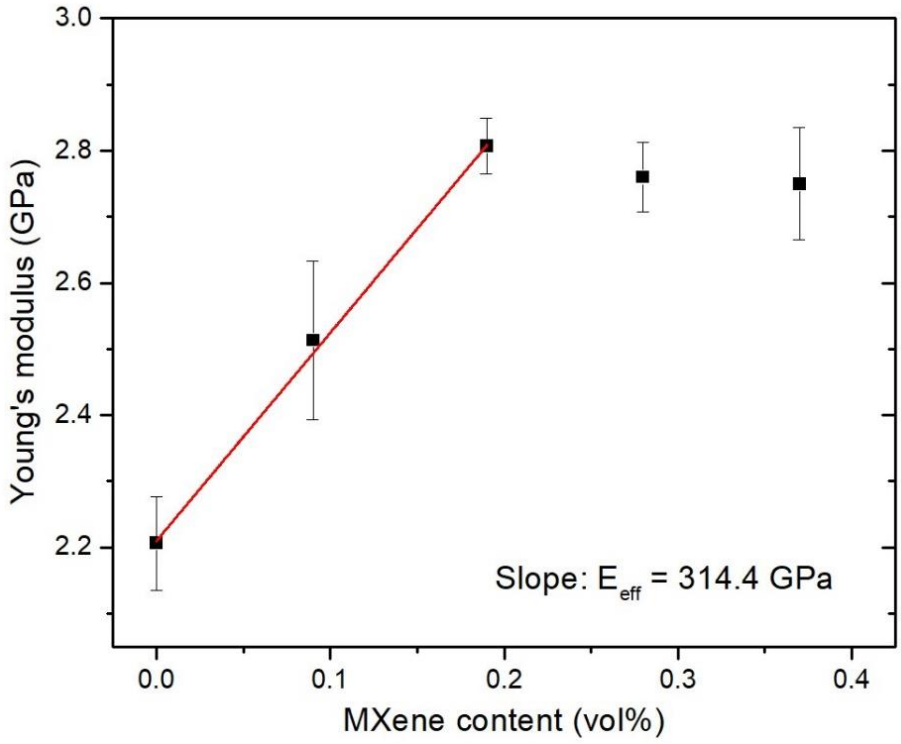

Figure S9. Variation of the Young's modulus of the nanocomposites with filler loading. The effective Young's modulus of the filler (E_{eff}) was determined to be 314.4 GPa.

References

[1] Liang JJ, Huang Y, Zhang L, Wang Y, Ma YF, Guo TY, et al. Molecular-Level Dispersion of Graphene into Poly(vinyl alcohol) and Effective Reinforcement of their Nanocomposites. Adv Funct Mater. 2009;19:2297-302.

[2] Zhao X, Zhang QH, Chen DJ, Lu P. Enhanced Mechanical Properties of Graphene-Based Poly(vinyl alcohol) Composites. Macromolecules. 2010;43:2357-63.

[3] Wang WM, Li ZL, Marsden AJ, Bissett MA, Young RJ. Mechanisms of reinforcement of PVA-Based nanocomposites by hBN nanosheets. Compos Sci Technol. 2022;218:8.